Nanoscale Imaging of Buried Structures with Elemental Specificity Using Resonant X-Ray Diffraction Microscopy

Changyong Song,[1] Raymond Bergstrom,[1] Damien Ramunno-Johnson,[1] Huaidong Jiang,[1] David Paterson,[2] Martin D. de Jonge,[3] Ian McNulty,[3] Jooyoung Lee,[4] Kang L. Wang,[4] and Jianwei Miao[1,*]

[1]*Department of Physics and Astronomy, University of California, Los Angeles, California 90095, USA*
[2]*Australian Synchrotron, 800 Blackburn Road, Clayton, VIC 3168, Australia*
[3]*Advanced Photon Source, Argonne National Laboratory, 9700 South Cass Avenue, Argonne, Illinois 60439, USA*
[4]*Department of Electrical Engineering, University of California, Los Angeles, California 90095, USA*

(Received 1 August 2007; published 18 January 2008)

We report the first demonstration of resonant x-ray diffraction microscopy for element specific imaging of buried structures with a pixel resolution of ~15 nm by exploiting the abrupt change in the scattering cross section near electronic resonances. We performed nondestructive and quantitative imaging of buried Bi structures inside a Si crystal by directly phasing coherent x-ray diffraction patterns acquired below and above the Bi M_5 edge. We anticipate that resonant x-ray diffraction microscopy will be applied to element and chemical state specific imaging of a broad range of systems including magnetic materials, semiconductors, organic materials, biominerals, and biological specimens.

DOI: 10.1103/PhysRevLett.100.025504 PACS numbers: 68.37.Yz, 41.50.+h, 61.05.cp, 61.72.uf

Much of our understanding of material behavior comes from detailed knowledge of its properties below the molecular scale [1]. While scanning probe microscopy and transmission electron microscopy can routinely image structures at atomic resolution [2,3], it remains a daunting task for nondestructive and quantitative imaging of buried structures on the nanometer scale with elemental and chemical specificity. X rays are ideally suited for element and chemical state specific imaging of buried structures due to their long penetration depth and the presence of core electron resonances in this energy region [4]. To date, a number of x-ray spectromicroscopes such as photoemission electron microscopes, x-ray fluorescence microscopes, scanning and transmission x-ray microscopes have been developed for imaging of magnetic materials, organic and biological specimens with elemental and chemical specificity [5–8]. However, the spatial resolution is currently limited by x-ray focusing optics. By using Fresnel zone plates, the smallest focal spot currently attainable is 30 nm for hard x rays [9] and 15 nm for soft x rays [10]. Furthermore, when the focal spot of soft x rays reaches 15 nm, the depth of focus becomes smaller than 0.5 μm [11], which limits the thickness of the sample under investigation. To overcome these obstacles, x-ray diffraction microscopy was developed for high-resolution imaging by avoiding the use of lenses (i.e., lensless imaging) [12]. The technique has yielded manifestly superior resolution in nondestructive and quantitative 2D and 3D imaging of materials and biological specimens [13–18]. Here, for the first time, we combine spectroscopy with lensless imaging and demonstrate resonant x-ray diffraction microscopy for quantitative and element specific imaging of buried structures at the nanometer scale.

Our method exploits the abrupt change of the x-ray atomic scattering factors in the vicinity of absorption edges to achieve elemental specificity. Coherent x-ray diffraction patterns were obtained just below and above the absorption edge of the target element. The difference of the reconstructed images represents the spatial distribution of the element. Figure 1 shows the schematic layout of a resonant x-ray diffraction microscope, mounted on a synchrotron undulator beam line. A grating monochromator and a pair of entrance and exit slits located far upstream of the microscope were used to control the temporal and spatial coherence of the x-ray beam. The monochromator system was designed such that a small change of the x-ray energy would not alter the beam position or direction. A 10-μm-diameter pinhole selected the spatially coherent part of the beam. The sample was mounted 50 mm downstream of the pinhole. A guard slit was positioned just in front of the sample to minimize parasitic scattering from the pinhole and upstream optical components. A liquid-nitrogen cooled CCD camera with 1024×1024 pixels, placed at a distance of 49 cm downstream of the sample, was used to record coherent x-ray diffraction patterns.

We applied the element specific imaging technique to map out Bi dopants inside a Si crystal. Despite their small concentration, dopant atoms often control the overall physical properties of materials. The precise manipulation of dopants has opened up new possibilities in designing advanced functional materials [19]. Bi among group-III and V semiconductors has attracted considerable attention due to its role as a superior surfactant with the smallest segregation coefficient and solid solubility. As a good surfactant, it is often used to facilitate the hetero-epitaxial growth of Si/Ge with sharp boundary, which is critical for the applications in optoelectronic devices [20,21]. The Bi doped Si film of 1 μm thick was grown by using molecular beam epitaxy to codeposit Bi and Si atoms together, after growing a Si:Ge buffer layer on a Si (001) wafer. As the

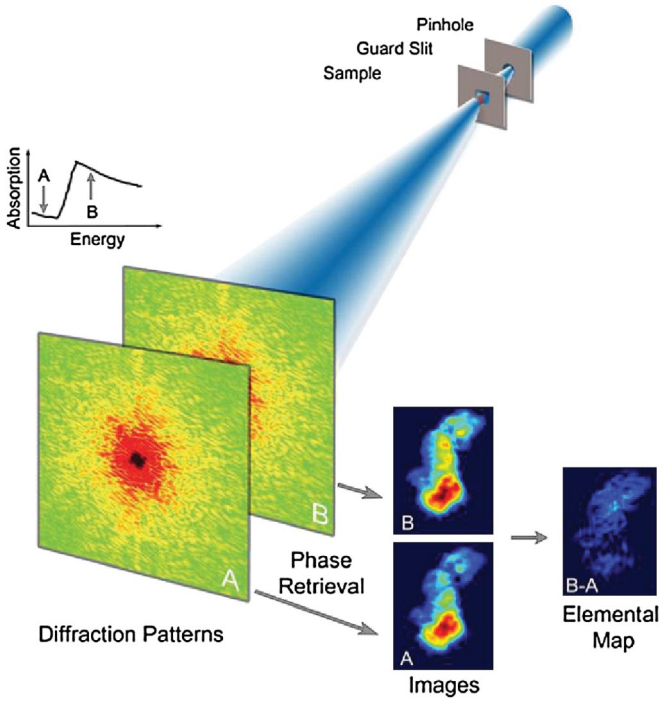

FIG. 1 (color). Schematic layout of the resonant x-ray diffraction microscope. Two diffraction patterns are acquired below and above the absorption edge of a specific element and are directly phased to obtain high-resolution images. The difference of the two images represents the spatial distribution of the specific element. The ultimate resolution of the microscope is limited only by the x-ray wavelengths and can in principle reach the atomic level.

growth temperature was relatively low (300 °C), most of Bi should be incorporated into the Si film [22]. The sample was heavily doped with a dopant density of $\sim 5 \times 10^{20}$ cm^{-3}. Before the x-ray diffraction experiment, the Si:Ge buffer layer was chemically dissolved to separate the doped Si layer from the Si wafer by using a poly-silicon etchant. The etchant solution was mixed in a ratio of 40:1:2:57 with HNO_3(70%):HF(49%):CH_3COOH:H_2O.

Coherent diffraction patterns were acquired from a Bi doped Si sample at x-ray energies of 2.550 keV and 2.595 keV, just below and above the Bi M_5 edge, respectively. As the sample thickness is about 3 times less than the attenuation length at these x-ray energies, the multiple scattering effect is negligible in our experiment. Figure 2(a) shows the x-ray diffraction pattern at 2.550 keV. The origin of the intense speckles is mainly due to the finite size and the surface morphology of the sample, where the speckle size is proportional to the inverse of the sample size. The zoom-in region shown in Fig. 2(b) is compared with the same region of the diffraction pattern obtained at 2.595 keV [Fig. 2(c)]. While the diffraction patterns overall look very similar, the lineouts shown in Fig. 2(d) indicate noticeable differences between the two patterns. Because they share the same sample boundary, the diffraction patterns possess the same speckle size. But the contrast difference of the speckles is due to the abrupt change of the real and imaginary components of the Bi atomic scattering factor, whereas the imaginary component is about 2.8 times larger at 2.595 keV than at 2.550 keV [23]. The difference becomes more noticeable at higher spatial frequency ($Q > 0.081/\text{nm}$), indicating that the change in index of refraction of the sample occurs on a shorter length scale (< 120 nm).

Because the atomic scattering factor of Bi is complex valued, the diffraction pattern is noncentrosymmetric as shown in Fig. 2(a). Complex-valued objects are in general more difficult to reconstruct than real objects [24]; we overcome this problem by using the guided hybrid-input-output algorithm (GHIO) [25,26]. The GHIO algorithm

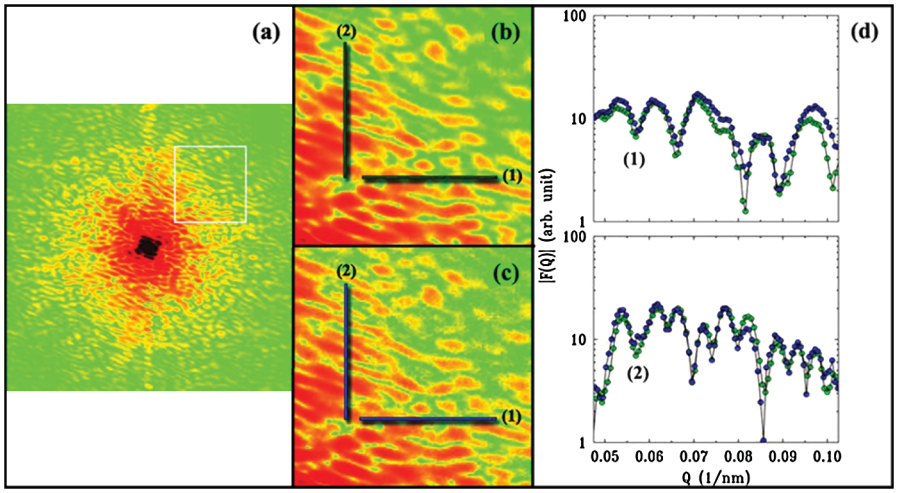

FIG. 2 (color). (a) Coherent x-ray diffraction pattern of a Bi doped Si crystal obtained at $E = 2.550$ keV. The missing center of the diffraction pattern is filled in by using the image reconstruction algorithm. (b) Zoom-in view of the white square region. (c) The same region of the diffraction pattern with $E = 2.595$ keV. (d) Lineout comparison of the two diffraction patterns. The green and blue curves correspond to $E = 2.550$ keV and 2.595 keV, respectively.

began with 20 independent reconstructions of each diffraction pattern with random phase sets as the initial input. Each reconstruction iterated back and forth between real and reciprocal space, while applying constraints in both domains. In real space, the pixel values outside of a support and the negative real or imaginary component of the pixel values inside the support were slowly pushed close to zero, where the support is a boundary larger than the envelope of the specimen. In reciprocal space, the phases were updated with each iteration, while the modulus of the Fourier transform was left unchanged. After 4000 iterations, 20 images were obtained, defined as the 0th generation. For each image, the R_F value was then calculated, which represents the difference between the modulus of the calculated and the measured Fourier modulus. By multiplying the image with the lowest R_F, the so-called seed, with each of the 20 images and taking the square root of the product, we obtained a new set of 20 images, which was used for the next generation. This step merged the best image in the current generation with each of the 20 images so that the ''favorable gene'' (i.e., the smallest R_F) would be passed on to the succeeding generations. We repeated the process in each generation. After 11 generations, the best 3 out of 20 images with the smallest R_F values were averaged to determine a tight support (i.e., the true boundary of the specimen). Using this tight support, we ran another 11 generations of GHIO to obtain 20 consistent images. The best 3 images with the smallest R_F values were averaged to obtain the final reconstructed image.

To assure the reliability of the reconstruction process, we carried out 2 independent GHIO runs for each coherent x-ray diffraction pattern. The independently reconstructed images were very consistent, from which we estimated the reconstruction error to be ~4.4% [27]. The reconstruction error (R_{real}) was determined by $R_{\text{real}} = \sum_{x,y}|\rho_1(x,y) - \rho_2(x,y)|/\sum_{x,y}|\rho_1(x,y) + \rho_2(x,y)|$, where $\rho_1(x,y)$ and $\rho_2(x,y)$ represent two independently reconstructed images for each coherent x-ray diffraction pattern. Figures 3(a) and 3(b) show the reconstructed images below and above the Bi M_5 edge with a pixel resolution of 14.5 nm. The pixel resolution (d) was determined based on $d = z\lambda/pN$, where z is the distance from the sample to the CCD, λ is the wavelength, p is the CCD pixel size, and N is the number of pixels with good diffraction signals. The two images were normalized based on the total x-ray flux and the atomic scattering factor of Bi and Si [23]. Figure 3(c) shows the difference of the two images, which represents the spatial distribution of the buried Bi dopant structure. Figure 4 shows the distribution of the Bi structure (yellow) along the dashed line in Fig. 3(c), obtained by subtracting the image below the Bi M_5 edge (green) from that above the edge (blue). The distribution of Bi structures is clearly distinguished from the reconstruction error of ~4.4%. An SEM image of the sample is shown in Fig. 3(d). The surface morphology of the SEM image is consistent with the x-ray images, which further verifies the fidelity of the image reconstruction process. The images acquired by the two techniques are markedly different, however. The x-ray diffraction microscope provides the index of refraction of the sample, projected along the incident x-ray direction, whereas the SEM shows only the surface structure of the sample.

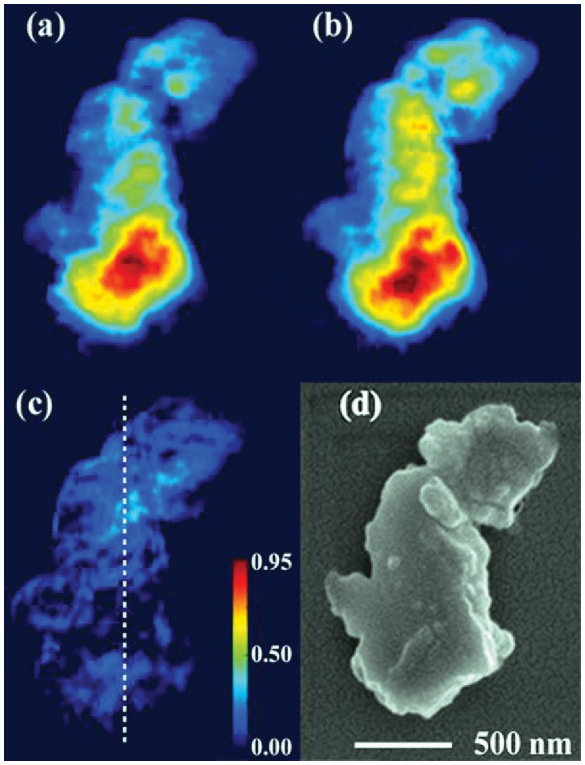

FIG. 3 (color). Elemental mapping of Bi structure showing (a) reconstructed image at $E = 2.550$ keV and (b) $E = 2.595$ keV, respectively. (c) Distribution of the Bi structure obtained by taking the difference of the two images, which represents a 2D projection of the 3D Bi distribution and therefore does not contain the depth information of the Bi distribution in the sample. (d) SEM image of the same sample.

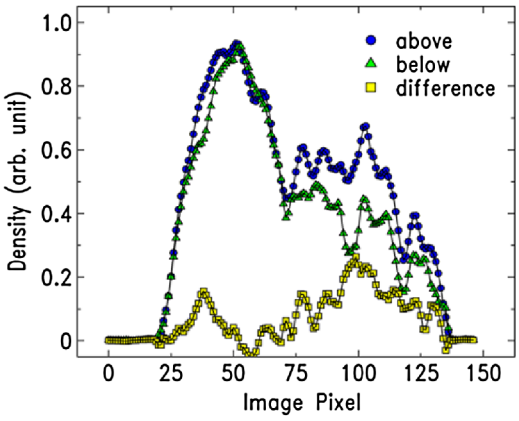

FIG. 4 (color online). Distribution of Bi structure along the dashed line in Fig. 3(c), obtained by subtracting the reconstructed image below the Bi M_5 edge from that above the edge.

Based on the elemental map of Bi dopants in Fig. 3(c), we observed that the Bi atoms are broadly dispersed, consistent with the weak segregation tendency. However, clusters of Bi atoms also appeared as shown in Figs. 3(c) and 4, implying that the atomic growth was influenced by non-negligible interlayer correlation among Bi atoms. The interlayer correlation can be attributed to a strong elastic strain caused by the size mismatch of Bi atoms which have an atomic volume almost 3 times larger than that of the host Si atoms. Our understanding of the 3D self-assembly of nanostructures up to now has mainly relied either on reciprocal-space analysis techniques such as diffuse x-ray scattering [28] or destructive characterization methods of TEM [3]. While the reciprocal-space approach studies averaged structure information, the x-ray diffraction microscope provides *ab initio* information of local structures on the nanometer scale. We expect that this novel imaging technique can be used to gain in-depth understanding of atomic growth on systematically prepared samples.

In summary, we demonstrated resonant x-ray diffraction microscopy at nanometer resolution by exploiting the abrupt change in the scattering cross section near electronic resonances. This was achieved by obtaining coherent x-ray diffraction patterns below and above the absorption edge of a specific element, and then taking the difference between the reconstructed images to obtain the elemental distribution. We performed nondestructive and quantitative imaging of buried Bi structures inside a micrometer-sized Si crystal. While we achieved a pixel resolution of 15 nm, the ultimate resolution is limited only by the x-ray wavelengths and can in principle reach the near atomic level. Resonant x-ray diffraction microscopy hence in principle opens a pathway to the detection of single dopant atoms. Moreover, this imaging technique is also sensitive to chemical states via near-edge resonances and can be extended to exploit other contrast mechanisms depending on resonant transitions such as x-ray magnetic circular dichroism [29]. Resonant x-ray diffraction microscopy can thus be adapted to perform electronic orbital as well as chemical state specific imaging of magnetic materials [4,8], semiconductors [30], organic materials [7], biominerals [31], and biological specimens [13,32,33]. While radiation damage may ultimately limit the attainable resolution of biological specimens, new sources such as x-ray free electron lasers will enable damage to be circumvented by acquiring the diffraction patterns on ultrafast time scales [16,34,35].

J. M. thanks A. Bienenstock for many stimulating discussions. This work was supported by the US DOE, BES (No. DE-FG02-06ER46276) and the US NSF (No. DMR-0520894). Use of the APS is supported by the US DOE, BES (No. DE-AC02-06CH11357).

*miao@physics.ucla.edu

[1] S. J. L. Billinge and I. Levin, Science **316**, 561 (2007).
[2] E. Meyer, S. P. Jarvis, and N. D. Spencer, MRS Bull. **29**, 443 (2004).
[3] J. C. H. Spence, *High-Resolution Electron Microscopy* (Oxford University Press, Oxford, 2003), 3rd ed.
[4] *Resonant Anomalous X-Ray Scattering: Theory and Applications*, edited by G. Materlik, C. J. Sparks, and K. Fischer (Elsevier, New York, 1994).
[5] F. Nolting *et al.*, Nature (London) **405**, 767 (2000).
[6] K. M. Kemner *et al.*, Science **306**, 686 (2004).
[7] H. Ade *et al.*, Science **258**, 972 (1992).
[8] P. Fischer *et al.*, Mater. Today **9**, 26 (2006).
[9] *X-Ray Microscopy: Proceedings of the 8th International Conference*, edited by S. Aoki, Y. Kagoshima, and Y. Suzuki, IPAP Conference Series Vol. 7 (IPAP, Tokyo, 2006).
[10] W. Chao *et al.*, Nature (London) **435**, 1210 (2005).
[11] C. Jacobsen, J. Kirz, and S. Williams, Ultramicroscopy **47**, 55 (1992).
[12] J. Miao *et al.*, Nature (London) **400**, 342 (1999).
[13] D. Shapiro *et al.*, Proc. Natl. Acad. Sci. U.S.A. **102**, 15 343 (2005).
[14] J. Miao *et al.*, Phys. Rev. Lett. **89**, 088303 (2002).
[15] M. A. Pfeifer *et al.*, Nature (London) **442**, 63 (2006).
[16] H. N. Chapman *et al.*, Nature Phys. **2**, 839 (2006).
[17] H. M. Quiney *et al.*, Nature Phys. **2**, 101 (2006).
[18] J. M. Rodenburg *et al.*, Phys. Rev. Lett. **98**, 034801 (2007).
[19] D. Kitchen *et al.*, Nature (London) **442**, 436 (2006).
[20] D. Kandel and E. Kaxiras, Phys. Rev. Lett. **75**, 2742 (1995).
[21] N. Paul *et al.*, Phys. Rev. B **69**, 193402 (2004).
[22] G. Fenga, K. Oe, and M. Yoshimoto, J. Cryst. Growth **301–302**, 121 (2007).
[23] B. L. Henke, E. M. Gullikson and J. C. Davis, At. Data Nucl. Data Tables **54**, 181 (1993).
[24] J. R. Fienup, J. Opt. Soc. Am. A **4**, 118 (1987).
[25] J. Miao *et al.*, Phys. Rev. Lett. **97**, 215503 (2006).
[26] C. C. Chen *et al.*, Phys. Rev. B **76**, 064113 (2007).
[27] See EPAPS Document No. E-PRLTAO-99-070753 for supplementary information. For more information on EPAPS, see http://www.aip.org/pubservs/epaps.html.
[28] G. Springholz *et al.*, Science **282**, 734 (1998).
[29] G. Schütz *et al.*, Phys. Rev. Lett. **58**, 737 (1987).
[30] International technology roadmap for semiconductors: 2005 (http://public.itrs.net).
[31] M. J. Glimcher, in *Metabolic Bone Disease*, edited by L. V. Avioli and S. M. Krane (Academic, New York, 1998).
[32] J. Miao *et al.*, Annu. Rev. Biophys. Biomol. Struct. **33**, 157 (2004).
[33] J. Miao *et al.*, Proc. Natl. Acad. Sci. U.S.A. **100**, 110 (2003).
[34] R. Neutze *et al.*, Nature (London) **406**, 752 (2000).
[35] J. Miao, K. O. Hodgson, and D. Sayre, Proc. Natl. Acad. Sci. U.S.A. **98**, 6641 (2001).